Applied Physics A (2020)126:102
https://doi.org/10.1007/s00339-019-3256-7

Applied Physics A
Materials Science & Processing

Caloric and isothermal equations of state of solids: empirical modeling with multiply broken power-law densities

Roman Tomaschitz[1]

Received: 14 October 2019 / Accepted: 20 December 2019

Abstract
Empirical equations of state (EoSs) are developed for solids, applicable over extended temperature and pressure ranges. The EoSs are modeled as multiply broken power laws, in closed form without the use of ascending series expansions; their general analytic structure is explained and specific examples are studied. The caloric EoS is put to test with two carbon allotropes, diamond and graphite, as well as vitreous silica. To this end, least-squares fits of broken power-law densities are performed to heat capacity data covering several logarithmic decades in temperature, the high- and low-temperature regimes and especially the intermediate temperature range where the Debye theory is of limited accuracy. The analytic fits of the heat capacities are then temperature integrated to obtain the entropy and caloric EoS, i.e. the internal energy. Multiply broken power laws are also employed to model the isothermal EoSs of metals (Al, Cu, Mo, Ta, Au, W, Pt) at ambient temperature, over a pressure range up to several hundred GPa. In the case of copper, the empirical pressure range is extended into the TPa interval with data points from DFT calculations. For each metal, the parameters defining the isothermal EoS (i.e. the density–pressure relation) are inferred by nonlinear regression. The analytic pressure dependence of the compression modulus of each metal is obtained as well, over the full data range.

Keywords Multi-parameter equation of state (EoS) · Caloric EoS of carbon allotropes · Specific heat of vitreous silica · Thermal EoS and compression modulus of metals · High-pressure regime · Multiply broken power laws

1 Introduction

The aim of this paper is to develop analytic equations of state (EoSs) for solids which can reproduce empirical data sets covering several orders in temperature and pressure, including the extended crossovers between the asymptotic low and high pressure and temperature regimes. The proposed EoSs are multiply broken power laws, which do not involve truncated series expansions in density, pressure or temperature (frequently used in empirical EoSs, cf. e.g. the reviews [1–5]) and are, therefore, equally suitable for the mentioned asymptotic regions.

At first, we study caloric EoSs, i.e. the temperature dependence of the internal energy, obtained by integration of the isochoric heat capacity. We work out three specific examples, obtaining closed analytic expressions for the heat capacities of diamond, graphite and vitreous silica by least-squares regression. The isochoric heat capacities are structured as multiply broken power laws [6–8],

$$C_V(T) = b_0 T^{\beta_0} \prod_{k=1}^{n} \left(1 + (T/b_k)^{\beta_k/|\eta_k|}\right)^{\eta_k} \tag{1}$$

with positive amplitudes b_0 and b_k, $k = 1, \ldots, n$, and $b_k << b_{k+1}$. The exponents β_k, $k = 1, \ldots, n$ are positive, β_0 is real, and the exponents η_k can be positive or negative. $C_V(T)$ is analytic on the positive real axis and consists of $n+1$ approximate power-law segments, $\propto T^{\beta_0}$, $T^{\beta_0+\beta_1 \mathrm{sign}(\eta_1)}, \ldots, T^{\beta_0+\sum_{k=1}^{n}\beta_k \mathrm{sign}(\eta_k)}$ in the intervals $T << b_1$, $b_1 << T << b_2, \ldots, b_n << T$, respectively. The amplitudes b_k define the break points between the power-law segments and the exponents η_k determine the extent of the transitional regions. Power laws in log–log plots appear as approximately straight segments, and the exponents η_k determine the extent of the transitional regions between the power-law segments.

The isochoric heat capacities of diamond, graphite and vitreous SiO_2, discussed in Sect. 2, are special cases of

✉ Roman Tomaschitz
tom@geminga.org

[1] Sechsschimmelgasse 1/21-22, 1090 Vienna, Austria

Published online: 16 January 2020

the broken power-law density (1). In the case of diamond, $C_V(T)$ interpolates between the constant Dulong–Petit high-temperature limit and the Debye T^3 low-temperature slope. In the intermediate temperature range, the broken power law (1) is sufficiently adaptable to model deviations from the Debye theory such as the boson peaks of glasses. In the case of graphite, $C_V(T)$ interpolates between the linear low-temperature slope of the degenerate electron gas and the classical Dulong–Petit regime, and in the case of the SiO_2 glass, the linear low-temperature slope is replaced by a power law with non-integer index close to one, generated by a fermionic two-level system. In the latter two examples, a phononic cubic temperature slope does not emerge in the empirical data sets, as the low-temperature regime is dominated by Fermi systems.

In recent years, new phenomenological EoSs have been proposed to model density–pressure data sets obtained from Hugoniot shock compression of, for instance, alkali metals [9, 10], alkaline earths [11], aluminum [12–14], iron [15], copper [16], tin [17] and tungsten [18], to mention but a few. In the second part of this paper, multiply broken power laws are employed as isothermal EoSs of metals, with emphasis on the high-pressure (GPa and TPa) regime. In this case, the pressure dependence of the mass density ρ has the analytic shape

$$\rho(P) = \rho_0 \prod_{k=1}^{n} \left(1 + P/b_k\right)^{\eta_k} \tag{2}$$

with positive amplitudes ρ_0, b_k, $b_k << b_{k+1}$, and real exponents η_k, $k = 1, \ldots, n$. These parameters are temperature dependent, but will be treated as constants in the examples studied here, at ambient temperature of 300 K. Density (2) consists of $n+1$ power-law segments, $\propto 1, P^{\eta_1}, \ldots, P^{\sum_{k=1}^{n}\eta_k}$, in the intervals $P << b_1$, $b_1 << P << b_2, \ldots, b_n << P$. In contrast to the broken power law (1), we have put $\beta_0 = 0$ and $\beta_k = |\eta_k|$ in (2), so that $\rho(P)$ is analytic at $P = 0$, which is essential to model the compression modulus in the low-pressure range consistent with ultrasonic measurements. When discussing the compression modulus in Sect. 3, we will also need the logarithmic derivative of density (2), $\rho'(P)/\rho(P) = \sum_{k=1}^{n} \eta_k/(P + b_k)$, to show how the low-pressure limit of EoS (2) is related to the Murnaghan EoS [19–24].

In Sect. 3, the EoS (2) will be put to test by performing least-squares fits to high-pressure data sets of Al, Cu, Mo, Ta, Au, W, and Pt, which cover an extended pressure range, from ambient (zero) pressure to several hundred GPa [25–27]. In the case of copper, the available experimental pressure range (up to 450 GPa [26]) will be extended with data sets obtained from DFT calculations [28]. The least-squares fit of the EoS of copper then covers pressures reaching 60 TPa. In Sect. 4, we present our conclusions.

2 Heat capacity, caloric EoS, and entropy of diamond, graphite and vitreous silica

In this section, the modeling of empirical heat capacity data by multiply broken power-law densities is discussed. Two carbon allotropes, diamond and graphite, and a glass, v - SiO_2, are studied as specific examples. Explicit formulas for the molar isochoric heat capacities are obtained by

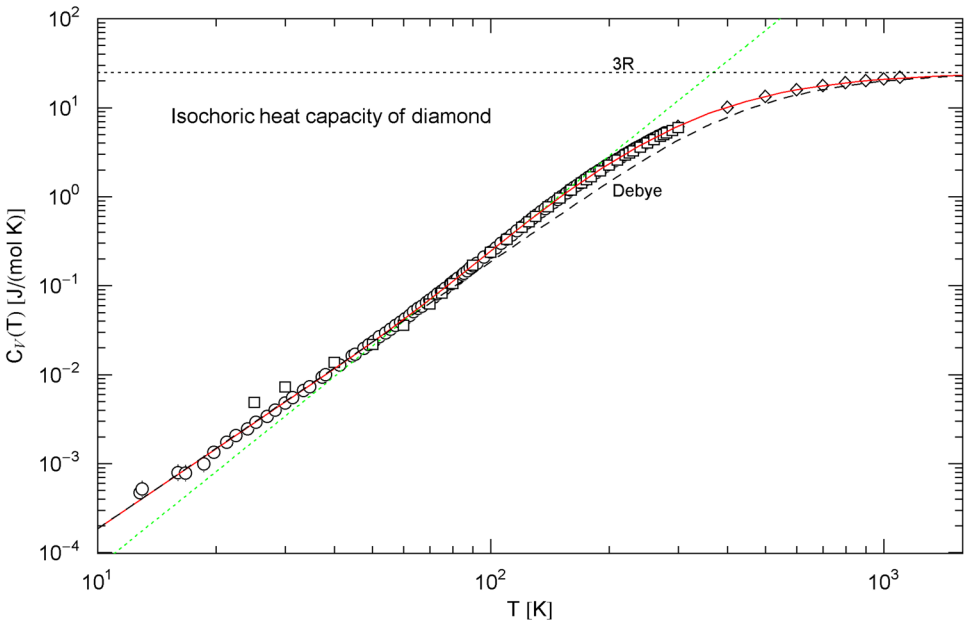

Fig. 1 Isochoric heat capacity of diamond, cf. Sect. 2.1. Data points from Ref. [33] (circles), Ref. [34] (squares) and Ref. [35] (diamonds). The χ^2 fit (solid red curve) is performed with $C_V(T)$ in (3), the fitting parameters are recorded in Table 1. For comparison, the black dashed curve is the Debye approximation (4), with constant Debye temperature of $\theta_{\text{diamond}} = 2186$ K. The classical $3R$ Dulong–Petit limit is indicated by the black dotted line. The green dotted straight line depicts the tangent cT^κ at the inflection point ($T = 95.53$ K, $C_V = 0.2085$ J/(mol K)), with slope $\kappa = 3.547$ and amplitude $c = 1.972 \times 10^{-8}$ J/(mol $K^{1+\kappa}$))

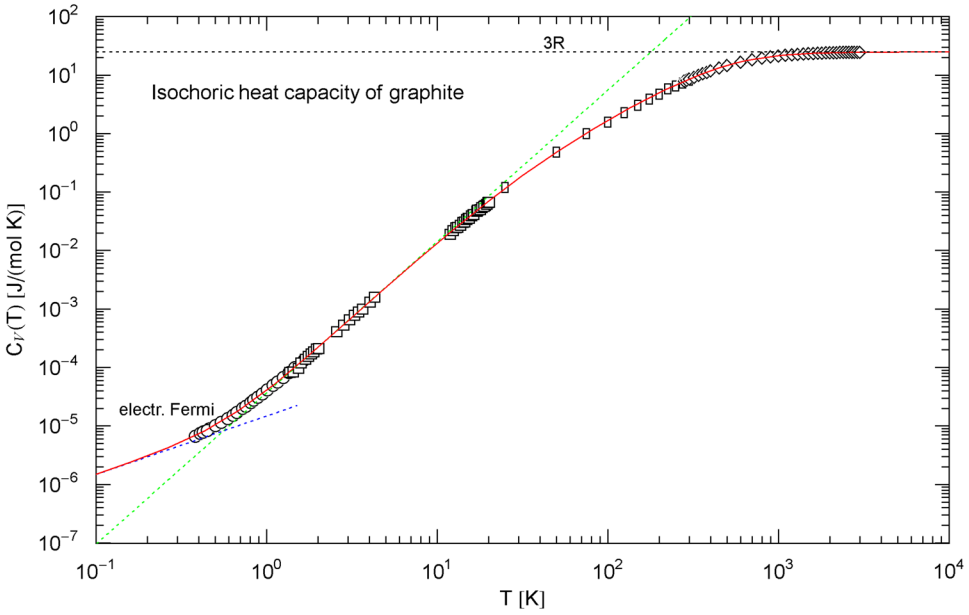

Fig. 2 Isochoric heat capacity of graphite, cf. Section 2.2. Data points from Ref. [36] (circles, Madagascar natural graphite), Ref. [37] (squares, Canadian natural graphite), Ref. [38] (rectangles, Acheson graphite), and Ref. [39] (diamonds, Acheson graphite). The experimental isobaric C_P data points have been converted into isochoric C_V points, cf. (6). The χ^2 fit (red solid curve) is performed with the analytic broken power law $C_V(T)$ in (7), the fitting parameters are listed in Table 1. The dotted blue asymptote $C_V \sim b_0 T$ is the low-temperature limit of the heat capacity of the electron plasma. The $C_V(T)$ curve has an inflection point at $T = 3.146\,\mathrm{K}$, $C_V = 7.170 \times 10^{-4}\,\mathrm{J/(mol\,K)}$. The dotted green line is the tangent cT^κ at the inflection point, with amplitude $c = 3.702 \times 10^{-5}\,\mathrm{J/(mol\,K^{1+\kappa})}$ and slope $\kappa = 2.586$, which is the maximum slope attained. See also Fig. 4 for the Debye approximation

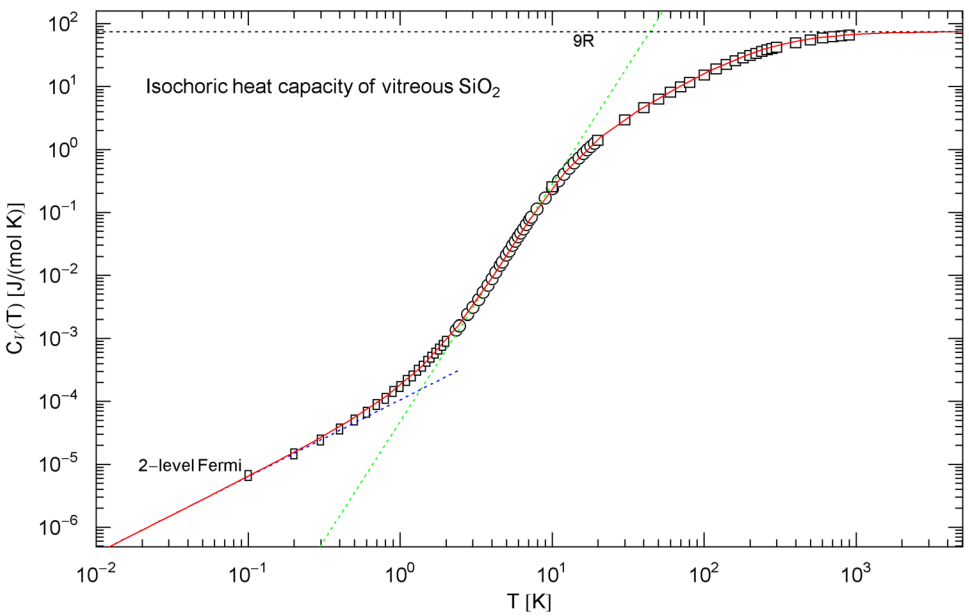

Fig. 3 Isochoric heat capacity of v - SiO_2, cf. Section 2.3. Data points from Ref. [45] (rectangles), Ref. [46] (circles), and Ref. [47] (squares). The least-squares fit (red solid curve) is performed with the broken power law $C_V(T)$ in (8), the fitting parameters are recorded in Table 1. The classical $9R$ limit is indicated by the black dotted line. The dotted blue low-temperature asymptote $C_V \sim b_0 T^{1.22}$ depicts the heat capacity of the two-level Fermi system discussed in Sect. 2.3, which dominates the phononic heat capacity at low temperature. The tangent cT^κ at the inflection point ($T = 5.240\,\mathrm{K}$, $C_V = 2.480 \times 10^{-2}\,\mathrm{J/(mol\,K)}$) has slope $\kappa = 3.770$ and amplitude $c = 4.815 \times 10^{-5}\,\mathrm{J/(mol\,K^{1+\kappa})}$

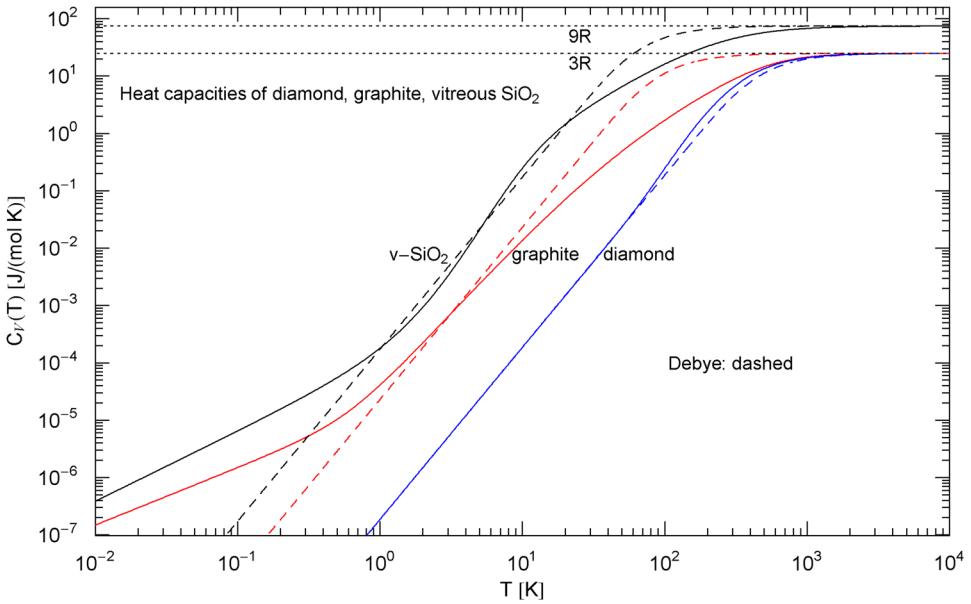

Fig. 4 Comparison of the molar isochoric heat capacities $C_V(T)$ of diamond, graphite and vitreous silica. The blue, red and black solid curves show the broken power laws $C_V(T)$ in (3), (7) and (8), respectively, with fitting parameters in Table 1. (The fits are depicted in Figs. 1, 2 and 3). The dashed curves are the Debye heat capacities, cf. (4). The Debye temperature of diamond is $\theta_{\text{diamond}} = 2186\,\text{K}$ ($c_D = b_0$, cf. (4) and Table 1), inferred from the low-temperature limit $C_V \sim b_0 T^3$ of the broken power law (3). The Debye temperatures $\theta_{\text{graphite}} = 438.7\,\text{K}$ and $\theta_{\text{v - SiO}_2} = 323.4\,\text{K}$ have been chosen so that the Debye heat capacity (4) intersects the fitted $C_V(T)$ curves at their inflection point, since the empirical heat capacities of graphite and v - SiO_2 do not exhibit a T^3 slope in any temperature range

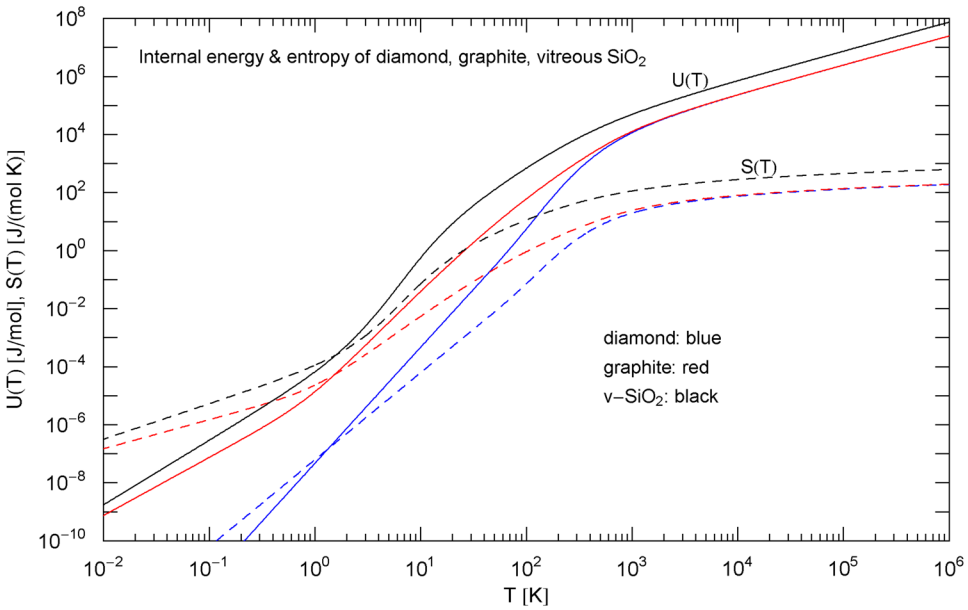

Fig. 5 Caloric EoS $U(T) = \int_0^T C_V \mathrm{d}T$ and molar entropy $S(T) = \int_0^T (C_V/T)\mathrm{d}T$ of diamond, graphite and vitreous silica, cf. (5). The caloric EoSs (thermal component of the internal energy) are depicted as solid curves, the entropies as dashed ones. At high temperature, $U(T) \propto T$ and the entropy diverges logarithmically. The isochoric heat capacities in the integrands are defined in (3), (7) and (8), with fitting parameters in Table 1. The low-temperature slopes read $U(T) \propto T^{1+\beta_0}$ and $S(T) \propto T^{\beta_0}$, with exponent β_0 in Table 1

nonlinear least-squares regression, cf. Figs. 1, 2 and 3. Comparisons with the Debye theory are depicted in Fig. 4. The temperature variation of the internal energy and entropy variables obtained from the regressed heat capacities is shown in Fig. 5. Alternative attempts to find caloric EoSs for diamond and graphite are discussed in Refs. [29–32] and references therein.

2.1 Diamond

We perform a χ^2 fit to the available data sets [33–35] of the diamond heat capacity, depicted in the double-logarithmic plot in Fig. 1, by employing a broken power law of type (1) as isochoric heat capacity,

Table 1 Fitting parameters of the molar isochoric heat capacity $C_V(T)$ of diamond, graphite and vitreous silica, see Figs. 1, 2 and 3

	Diamond	Graphite	v - SiO_2
b_0	1.8605×10^{-7}	1.4843×10^{-5}	1.0618×10^{-4}
b_1[K]	67.435	0.60277	2.6677
b_2[K]	282.02	40.466	10.585
b_3[K]	–	562.35	247.30
β_0	3	1	1.22
β_1	1.2496	1.6796	4.3172
β_2	$\beta_0 + \beta_1$	1.3235	4.0656
β_3	–	$\beta_0 + \beta_1 - \beta_2$	$\beta_0 + \beta_1 - \beta_2$
η_1	0.30536	0.69130	2.7558
η_2	2.1816	1.1347	1.7243
η_3	–	0.56727	0.93528
χ^2	0.144	0.0539	0.0635
dof	117–5	114–8	78–8
SE	0.070	0.070	0.431
$1 - R^2$	2.41×10^{-4}	5.55×10^{-5}	5.16×10^{-4}

The listed parameters (amplitudes b_i, exponents β_i, η_i) define the multiply broken power laws (3) (for diamond), (7) (graphite) and (8) (vitreous SiO_2) representing the empirical heat capacities. Some of these parameters are interrelated, cf. Sect. 2. b_0 is in units of $\mathrm{J/(K^{1+\beta_0}\,mol)}$. Also recorded are the minimum of the least-squares functional $\chi^2 = \sum_{i=1}^{N} (C_V(T_i) - C_{Vi})^2/C_{Vi}^2$ and the degrees of freedom (dof: number N of data points (T_i, C_{Vi}) minus number of independent fitting parameters). The standard error of the fits, $\mathrm{SE} = (\sum_{i=1}^{N} (C_V(T_i) - C_{Vi})^2/N)^{1/2}$, and the coefficient of determination, $R^2 = 1 - \sum_{i=1}^{N} (C_V(T_i) - C_{Vi})^2/(N\sigma^2)$, with sample variance $\sigma^2 = \sum_{i=1}^{N} (C_{Vi} - \bar{C}_V)^2/N$ and mean $\bar{C}_V = \sum_{i=1}^{N} C_{Vi}/N$, are listed as well

$$C_V(T) = b_0 T^3 (1 + (T/b_1)^{\beta_1/\eta_1})^{\eta_1} \frac{1}{(1 + (T/b_2)^{\beta_2/\eta_2})^{\eta_2}} \tag{3}$$

with amplitudes $b_1 << b_2$. The exponents $\beta_i, \eta_i, i = 1, 2$ are positive, and $\beta_2 = 3 + \beta_1$, so that the classical Dulong–Petit limit $C_V(T \to \infty) \sim 3R$ is recovered, with gas constant $R = 8.314$ J/(K mol). This limit also requires amplitudes in (3) related by $b_0 = 3R b_1^{\beta_1}/b_2^{\beta_2}$. The low-temperature limit is $C_V(T \to 0) \sim b_0 T^3$; the units used are C_V[J/(K mol)], b_0[J/($\mathrm{K^4}$ mol)], and b_i[K].

Broken power laws composed of multiple factors $(1 + (T/b_i)^{\beta_i/|\eta_i|})^{\eta_i}$ are quite efficient for data sets stretching over several decades in temperature, as demonstrated in the subsequent examples. In (3), we have three successive power laws, $\propto T^3$, $T^{3+\beta_1}$, $T^{3+\beta_1-\beta_2}$, in the intervals $T << b_1$, $b_1 << T << b_2$ and $b_2 << T$, respectively, which appear as approximately straight segments in log–log plots, and the exponents η_1, η_2 determine the transitional regions around the break points b_1 and b_2. The parameters b_1, b_2, η_1, η_2 and β_1 obtained from the least-squares fit are recorded in Table 1. In contrast to the Debye heat capacity, cf. (4), the heat capacity of diamond exhibits an inflection point in the crossover region between the low- and high-temperature regimes, see Fig. 1; the tangent of C_V at the inflection point is shown as green dotted line depicting the power law $\propto T^{3.547}$.

In Figs. 1 and 4, we have also indicated the Debye approximation,

$$C_D(T) = 9 n_{a/m} R \left[4D(\theta/T) - \frac{\theta/T}{\mathrm{e}^{\theta/T} - 1} \right], \quad D(x) := \frac{1}{x^3} \int_0^x \frac{y^3 \mathrm{d}y}{\mathrm{e}^y - 1},$$
$$\theta = \left(\frac{12}{5} \pi^4 \frac{n_{a/m} R}{c_D} \right)^{1/3}. \tag{4}$$

The asymptotic limits of the Debye function are $D(x >> 1) \sim \pi^4/(15x^3)$ and $D(x << 1) \sim 1/3$, so that $C_D(T \to 0) \sim c_D T^3$ and $C_D(T \to \infty) \sim 3 n_{a/m} R$, where $n_{a/m}$ denotes the number of atoms per molecule. The units are c_D[J/($\mathrm{K^4}$ mol)] and C_D[J/(K mol)] as above. The amplitude c_D is taken from the least-squares fit of $C_V(T)$ in (3), $c_D = b_0$, cf. Table 1, to recover the cubic low-temperature slope. Accordingly, the Debye temperature (4) of diamond is $\theta = 2186$ K. The low-temperature amplitude c_D is the only adjustable parameter of the Debye heat capacity, so that it is not surprising that the Debye approximation becomes inaccurate in the crossover region.

The temperature dependence of the caloric EoS (molar internal energy with zero-point energy subtracted) and molar entropy of diamond,

$$U(T)[\mathrm{J/\ mol}] = \int_0^T C_V \mathrm{d}T, \quad S(T)[\mathrm{J/(K\ mol)}] = \int_0^T \frac{C_V}{T} \mathrm{d}T \tag{5}$$

is shown in Fig. 5, calculated by substituting $C_V(T)$ in (3) with fitting parameters recorded in Table 1.

2.2 Graphite

The heat capacity data of graphite tabulated in the experimental papers [36–39] refer to the isobaric heat capacity C_P. The conversion of isobaric (at ambient pressure) to isochoric heat capacities C_V is done with the approximate formula $C_V \approx C_P/(1 + 0.526\, T\alpha_\perp(T))$, where 0.526 is the dimensionless Grüneisen constant of graphite [40] and $\alpha_\perp$ the thermal expansion coefficient perpendicular to the basal plane, cf. Refs. [40–42],

$$\begin{aligned}
\alpha_\perp(0 \le T \le 80) &= 5.35 \times 10^{-9} T^2 - 3.755 \times 10^{-11} T^3, \\
\alpha_\perp(80 \le T \le 273) &= 2.435 \times 10^{-7} T - 7.69 \times 10^{-10} T^2 \\
&\quad + 8.875 \times 10^{-13} T^3, \\
\alpha_\perp(273 \le T \le 1100) &= 2.722 \times 10^{-5} + 3.05 \times 10^{-9} (T - 273), \\
\alpha_\perp(1100 \le T \le 3000) &= 2.975 \times 10^{-5} + 9.604 \times 10^{-9} (T - 1100).
\end{aligned} \tag{6}$$

The units are $\alpha_\perp[1/\mathrm{K}]$ and $T[\mathrm{K}]$. The expansion $\alpha_{||}$ in the basal plane is negligible compared with $\alpha_\perp$. In the case of diamond, cf. Sect. 2.1, the conversion to isochoric heat capacities has already been done in the experimental papers. In the case of vitreous silica, cf. Sect. 2.3, $C_V \approx C_P$ in the temperature range of the available data points.

The heat capacity of graphite has an electronic and a phonon component, cf. Fig. 2; at low temperature, the linear electronic heat capacity overpowers the phonon component. For the least-squares fit depicted in Fig. 2, we use a broken power law similarly structured as in (3):

$$C_V(T) = b_0 T(1+(T/b_1)^{\beta_1/\eta_1})^{\eta_1} \times \frac{1}{(1+(T/b_2)^{\beta_2/\eta_2})^{\eta_2}} \frac{1}{(1+(T/b_3)^{\beta_3/\eta_3})^{\eta_3}}, \tag{7}$$

where the factors are ordered by increasing magnitude of the amplitudes, $b_1 << b_2 << b_3$, and the exponents β_i, η_i, $i = 1,2,3$, are positive. We put $\beta_3 = 1+\beta_1-\beta_2$ so that $C_V(T\to\infty) \sim 3R$, which also requires amplitudes related by $b_0[\mathrm{J/(K^2\ mol)}] = 3Rb_1^{\beta_1}/(b_2^{\beta_2}b_3^{\beta_3})$. The fitting parameters are b_i, η_i, $i = 1,2,3$, and β_1, β_2, cf. Table 1. The tangent at the inflection point of $C_V(T)[\mathrm{J/(K\ mol)}]$ is depicted as dotted green line $\propto T^{2.586}$ in Fig. 2, and the electronic low-temperature asymptote $C_V(T) \sim b_0 T$ is also shown in this figure.

There is no indication of a T^3 slope anywhere to be seen in the data set in Fig. 2. Therefore, we choose the amplitude c_D defining the Debye temperature in a way that the low-temperature T^3 slope of the Debye curve $C_D(T)$ [stated in (4)] cuts through the inflection point of the empirical heat capacity $C_V(T)$, see Fig. 4. This gives a Debye temperature of $\theta = 438.7$ K [with $c_D = 2.303\times10^{-5}\,\mathrm{J/(K^4\ mol)}$ in (4)]. A different choice of θ would just shift the T^3 slope parallel to the depicted slope. It is evident from Fig. 4 that the standard Debye approximation (4) cannot give a reasonable fit to the heat capacity of graphite, irrespective of the choice of θ, except at very high temperature; see also Ref. [41] and references therein for modifications of the Debye theory regarding graphite. The internal energy and entropy functions of graphite are shown in Fig. 5, obtained by integrating the empirical $C_V(T)$ in (7) (with fitting parameters in Table 1) according to Eq. (5).

2.3 Vitreous SiO_2

For the heat capacity of vitreous silica [43–47], we use a broken power law similar to that of graphite:

$$C_V(T) = b_0 T^{\beta_0}(1+(T/b_1)^{\beta_1/\eta_1})^{\eta_1} \times \frac{1}{(1+(T/b_2)^{\beta_2/\eta_2})^{\eta_2}} \frac{1}{(1+(T/b_3)^{\beta_3/\eta_3})^{\eta_3}}, \tag{8}$$

where the positive amplitudes $b_i[\mathrm{K}]$ are ordered by increasing magnitude, $b_1 << b_2 << b_3$. The exponents β_i and η_i, $i = 1,2,3$, are positive, and we put $\beta_3 = \beta_0+\beta_1-\beta_2$ so that $C_V(T\to\infty) \sim 9R$, which also requires $b_0[\mathrm{J/(K^{1+\beta_0}\ mol)}] = 9Rb_1^{\beta_1}/(b_2^{\beta_2}b_3^{\beta_3})$. The data points in Fig. 3 refer to the total heat capacity of the phonons and the fermionic two-level system which dominates the phonon heat capacity of the glass at low temperature [48, 49]. The low-temperature heat capacity of the two-level system is slightly different from linear, with power-law exponent of $\beta_0 = 1.22$ for v - SiO_2 [43, 44]. In the least-squares fit depicted in Fig. 3, we take this exponent β_0 as input parameter in (8); the low-temperature limit of (8) is $C_V[\mathrm{J/(K\ mol)}] \sim b_0 T^{\beta_0}$. The fitting parameters are b_i, η_i, $i = 1,2,3$, and β_1, β_2, cf. Table 1. The tangent of C_V at the inflection point is shown as dotted green line $\propto T^{3.770}$ in Fig. 3.

The Debye approximation $C_D(T)$ of the v - SiO_2 heat capacity is depicted in Fig. 4, cf. (4). As in the case of graphite, there is no T^3 slope visible in the measured heat capacity. The Debye temperature $\theta = 323.4$ K [$c_D = 1.724\times10^{-4}\,\mathrm{J/(K^4\ mol)}$ in (4)] is chosen so that $C_D(T)$ intersects the empirical heat capacity $C_V(T)$ [in (8)] at the inflection point. For comparison, the heat capacities $C_V(T)$ of diamond and graphite, cf. (3), (7) and Table 1, are also indicated in Fig. 4. The molar internal energy and entropy of v - SiO_2 are depicted in Fig. 5, calculated via (5) and (8).

To quantify the two-level system defining the heat capacity at low temperature [48, 49], we use a Fermi distribution with zero chemical potential and a power-law mode density. The spectral density and the internal energy then read

$$\mathrm{d}\rho(E) = a_0 \frac{E^{\beta_0-1}\mathrm{d}E}{\mathrm{e}^{E/T}+1}, \tag{9}$$

$$U(T) = \int_0^\infty E\mathrm{d}\rho(E) = a_0 T^{1+\beta_0}(1-2^{-\beta_0})\Gamma(1+\beta_0)\zeta(1+\beta_0) \tag{10}$$

with positive exponent β_0 and amplitude a_0 to be determined from heat capacity measurements. $\Gamma(x)$ and $\zeta(x)$ denote the gamma function and Riemann zeta function, cf. e.g. Ref. [50], and we have put $\hbar = k_B = 1$. The heat capacity is $C_V = U'(T) = (1+\beta_0)U/T$. By comparing with the low-temperature limit $C_V \sim b_0 T^{\beta_0}$ of the empirical heat capacity (8), we can specify the exponent $\beta_0 = 1.22$ and the amplitude in (9),

$$a_0 = \frac{b_0}{(1-2^{-\beta_0})\Gamma(2+\beta_0)\zeta(1+\beta_0)} \tag{11}$$

with b_0 in Table 1, so that $a_0 = 5.089\times10^{-5}\mathrm{J/(K^{2.22}\ mol)}$. The partition function is related to the internal energy by

$$\log Z = a_0 \int_0^\infty \log(1+\mathrm{e}^{-E/T}) E^{\beta_0-1}\mathrm{d}E = \frac{1}{\beta_0}\frac{U}{T}, \tag{12}$$

where we used integration by parts, and the entropy reads $S = \log Z + U/T = C_V/\beta_0$.

The spectral density $\mathrm{d}\rho(E)$ in (9) can be written in the equivalent quasi-particle momentum representation

$$\mathrm{d}\hat{\rho}(p) = \frac{4\pi s}{(2\pi)^3}\frac{p^2\mathrm{d}p}{\mathrm{e}^{E(p)/T}+1}, \quad U = \int_0^\infty E(p)\mathrm{d}\hat{\rho}(p), \tag{13}$$

where $s = 2$ is the spin degeneracy and

$$E(p) = c_0 p^{3/\beta_0},\ c_0 := (\frac{4\pi s}{(2\pi)^3}\frac{\beta_0}{3a_0})^{1/\beta_0} \tag{14}$$

is the power-law dispersion relation. Density (13) can be derived by box quantization; the dispersion relation (14) is to be regarded as the leading order of an ascending power series, and the thermodynamic variables derived from (9) or (13) are asymptotic low-temperature limits.

In Sects. 2.1–2.3, we have studied heat capacities and caloric EoSs obtained by fitting broken power laws (1) to empirical data. In the next section, we will use broken power-law densities to model isothermal EoSs of solids at high pressure, as indicated in (2).

3 Isothermal EoS of metals at high pressure

We start with the Murnaghan EoS $P = (K_0/K_0')((\rho/\rho_0)^{K_0'} - 1)$, cf. e.g. Refs. [19, 51, 52], where K_0 denotes the bulk modulus $K(P)$ at zero pressure and K_0' its pressure derivative at $P = 0$ (practically ambient pressure). $\rho(P)$ denotes the mass density and ρ_0 the mass density at zero pressure. The temperature dependence of $\rho(P)$, $K(P)$ and of the constants K_0, K_0', ρ_0 will not be explicitly indicated; the data sets studied here refer to a constant ambient temperature of 300 K. Inverting the above EoS, we find $\rho(P)/\rho_0 = (1 + PK_0'/K_0)^{1/K_0'}$ and the compressibility $\kappa_T := \rho'(P)/\rho(P) = 1/(K_0 + K_0'P)$, which gives a linear pressure dependence of the compression modulus $K(P) = 1/\kappa_T = K_0 + K_0'P$. Accordingly, $(\rho(P)/\rho'(P))_{|P=0} = K_0 = K(P)_{|P=0}$ and $(\rho(P)/\rho'(P))'_{|P=0} = K_0' = K'(P)_{|P=0}$. This linear relation and the Murnaghan EoS are usually applicable up to pressures of a few GPa, cf. e.g. Ref. [53].

To obtain density–pressure relations extending into the high-pressure range, we write the broken power-law density (2) as

$$\frac{\rho(P)}{\rho_0} = \left(1 + \frac{\hat{K}_0'}{\hat{K}_0}P\right)^{1/\hat{K}_0'} \prod_{k=2}^{n}\left(1 + P/b_k\right)^{\eta_k}, \tag{15}$$

where we have put $b_1 = \hat{K}_0/\hat{K}_0'$ and $\eta_1 = 1/\hat{K}_0'$. The first factor in (15) is modeled after the inverted Murnaghan EoS. The amplitudes in (15) are ordered according to $b_k << b_{k+1}$, see after (2). For pressures up to several hundred GPa (achievable in current shock compression experiments), two factors [$n = 2$ in (15)] suffice to obtain an accurate density–pressure relation. In this case, the EoS (15) is composed of three successive power laws, $\propto 1$, $P^{1/\hat{K}_0'}$, $P^{1/\hat{K}_0'+\eta_2}$, in the intervals $P << \hat{K}_0/\hat{K}_0'$, $\hat{K}_0/\hat{K}_0' << P << b_2$ and $b_2 << P$, respectively.

The compression modulus derived from EoS (15) reads

$$K(P) = \frac{\rho(P)}{\rho'(P)} = \frac{\hat{K}_0 + \hat{K}_0'P}{1+\Delta(P)}, \quad \Delta(P) := (\hat{K}_0 + \hat{K}_0'P)\sum_{k=2}^{n}\frac{\eta_k}{b_k}\frac{1}{1+P/b_k}, \tag{16}$$

where we made use of the logarithmic derivative of $\rho(P)$ stated after (2). $K(P)$ admits a Taylor expansion $K(P) = K_0 + K_0'P + \mathrm{O}(P^2)$ with coefficients

$$K_0 = \frac{\hat{K}_0}{1+\hat{K}_0 A}, \quad K_0' = \frac{\hat{K}_0' + \hat{K}_0^2 B}{(1+\hat{K}_0 A)^2}, \quad A := \sum_{k=2}^{n}\frac{\eta_k}{b_k}, \quad B := \sum_{k=2}^{n}\frac{\eta_k}{b_k^2}. \tag{17}$$

Accordingly, the parameters $\hat{K}_0$ and $\hat{K}_0'$ defining the first factor of EoS (15) are related to the bulk modulus at zero pressure, $K_0 = K(P)_{|P=0}$, and to its derivative $K_0' = K'(P)_{|P=0}$ by

$$\hat{K}_0 = \frac{K_0}{1-K_0 A}, \quad \hat{K}_0' = \frac{K_0' - K_0^2 B}{(1-K_0 A)^2}, \tag{18}$$

which is the inversion of (17). We substitute these relations for $\hat{K}_0$ and $\hat{K}_0'$ in EoS (15), so that the first factor of EoS (15) depends on the parameters K_0, K_0' and b_k, η_k, $k = 2, \ldots, n$. Evidently, if $|K_0 A| << 1$ and $|K_0^2 B/K_0'| << 1$, then $\hat{K}_0 \approx K_0$ and $\hat{K}_0' \approx K_0'$. The bulk modulus K_0 at zero pressure and its derivative K_0' are taken as measured input in EoS (15), inferred from acoustic low-pressure experiments. The amplitudes and exponents b_k, η_k, $k = 2, \ldots, n$ in EoS (15) are to be determined by least-squares regression. If ultrasonic measurements of K_0' are not available, we can take K_0' as additional fit parameter, and the same holds for K_0. As mentioned, the EoS (15) with two factors suffices for pressures up to several hundred GPa, so that only two fit parameters b_2, η_2 are needed for data sets presently obtainable by shock compression.

We test EoS (15) with pressure isotherms of Al (Fig. 6), Cu (Fig. 7), Mo (Fig. 8), Ta (Fig. 9), Au (Fig. 10), W (Fig. 11) and Pt (Fig. 12), all at ambient temperature of 300 K. The least-squares fits (red solid curves) are based on EoS (15) (with $n = 2$ and relations (18) substituted)

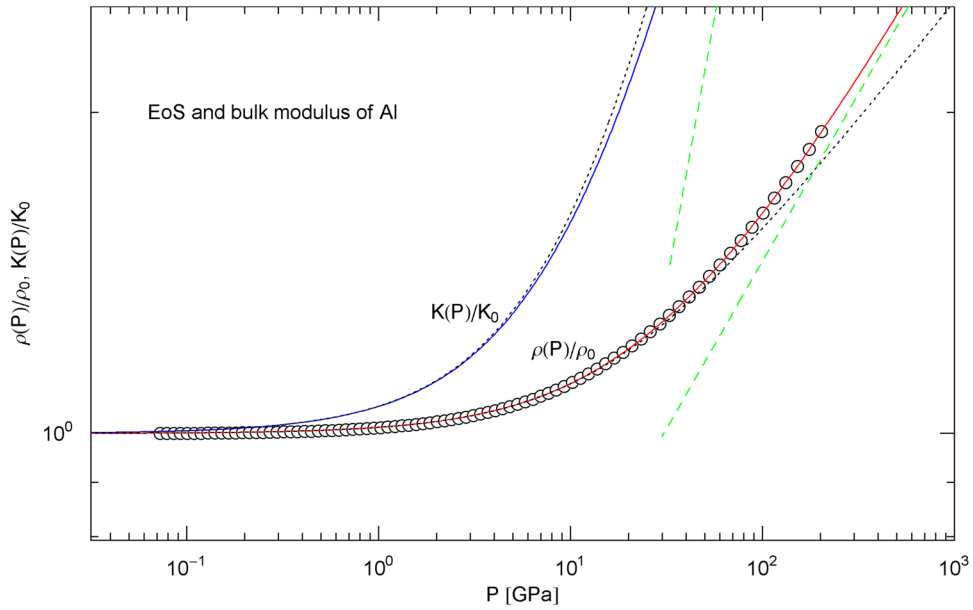

Fig. 6 Pressure isotherm at 300 K and compression modulus of aluminum. Data points up to 200 GPa (by Hugoniot shock compression) from Ref. [25]. The χ^2 fit (solid red curve) is performed with the isothermal EoS $\rho(P)$ in (15) ($n = 2$), the fitting parameters b_2, η_2 are recorded in Table 2. The solid blue curve depicts the compression modulus $K(P)$ calculated from the fitted EoS, cf. (16). ρ_0 and K_0 denote mass density and compression modulus at zero pressure, cf. Table 2. The dashed green lines are asymptotes to $\rho(P)/\rho_0$ and $K(P)/K_0$. The dotted black curves depict the Murnaghan approximations of the EoS and compression modulus, cf. after (18), calculated with K_0 and its derivative K_0' obtained from ultrasonic measurements, cf. Table 2

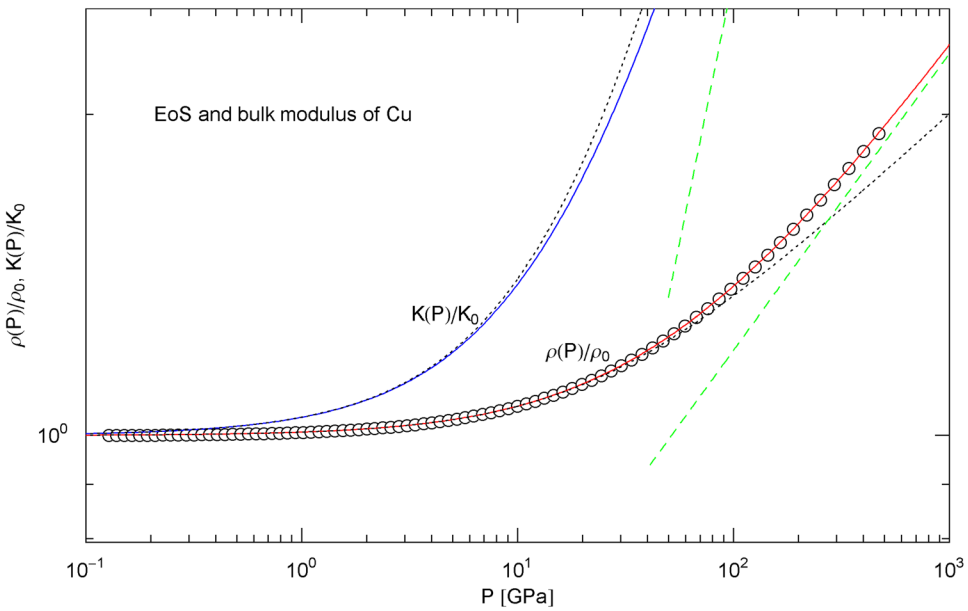

Fig. 7 Pressure isotherm and compression modulus of copper. Data points up to 450 GPa (via shockless compression) from Ref. [26]. The caption to Fig. 6 applies. The χ^2 fit (solid red curve) is performed with EoS $\rho(P)$ in (15), the fitting parameters are listed in Table 2. The solid blue curve shows the compression modulus $K(P)$, cf. (16). The dashed green lines are asymptotes. The dotted black curves depict the Murnaghan approximations, cf. after (18). See also Fig. 13 for the extension of the EoS into the TPa range

and data sets from Refs. [25–27]. The fit parameters b_2, η_2 and the input parameters ρ_0 and K_0, K_0' (the latter two obtained from ultrasonic measurements [54–65]) as well as the goodness-of-fit parameters (χ^2/dof, standard error, determination coefficient) are recorded in Table 2. In the case of Mo and Pt, K_0' is treated as a third fit parameter, for lack of ultrasonic estimates. In Fig. 13, the pressure range of copper (by shockless compression up to 450 GPa [26], cf. Figure 7) has been extended to 60 TPa using data points from DFT calculations [28], in which case a third factor can be specified in EoS (15) ($n = 3$), depending on two additional fit parameters b_3, η_3 recorded in the last column of Table 2.

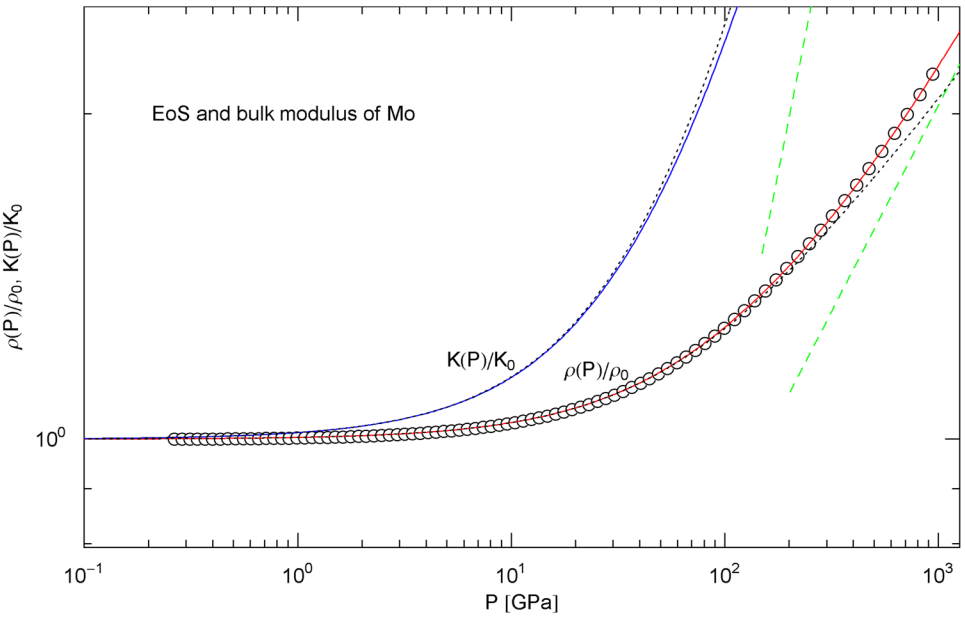

Fig. 8 Pressure isotherm and compression modulus of molybdenum. Data points up to 1 TPa (by shock compression) from Ref. [27]. The caption of Fig. 6 applies. The χ^2 fit (solid red curve) is performed with EoS $\rho(P)$ in (15) and fitting parameters in Table 2. The solid blue curve shows the compression modulus $K(P)$, cf. (16). The dashed green lines are asymptotes and the dotted black curves depict the Murnaghan approximations

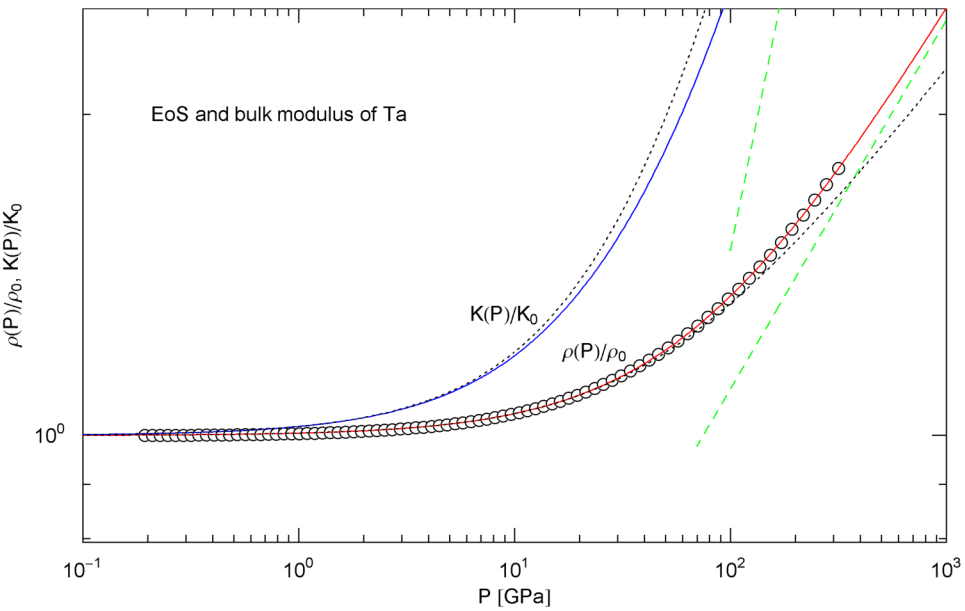

Fig. 9 Pressure isotherm and compression modulus of tantalum. Data points up to 300 GPa by shock compression [25]. The χ^2 fit (solid red curve) is performed with EoS $\rho(P)$ in (15) and fitting parameters in Table 2. The compression modulus $K(P)$, cf. (16), is depicted as blue solid curve. The dashed green lines are the asymptotes of $\rho(P)/\rho_0$ and $K(P)/K_0$. The dotted black curves depict the Murnaghan EoS and the linear compression modulus derived from it, cf. after (18)

In Figs. 6, 7, 8, 9, 10, 11, 12 and 13, we have also depicted the pressure dependence of the compression modulus $K(P)$ (solid blue curves) defined in (16), using input and fitting parameters of the regressed EoS (15) listed in Table 2. In these figures, we also compare the EoS (15) with the Murnaghan EoS $\rho_{\rm M}(P)/\rho_{\rm M0} = (1 + (K_0'/K_0)P)^{1/K_0'}$ outlined at the beginning of this section [we write here $\rho_{\rm M}(P)$ and $\rho_{\rm M0}$ for density and density at zero pressure to distinguish this EoS from the general EoS in (15)]. The compression modulus $K(P)$ in (16) is also compared with the linear relation $K_{\rm M}(P) = K_0 + K_0'P$ obtained from the Murnaghan EoS. (The linearity of $K_{\rm M}(P)$ is somewhat hidden in the log–log representation of the figures.) Actually, this linear relation, experimentally verified up to pressures of a few GPa (but usually invalid above 10 GPa, see Figs. 6, 7, 8, 9, 10, 11 and 12) is the starting point when deriving the Murnaghan EoS, by substituting $K_{\rm M}(P) = \rho_{\rm M}(P)/\rho_{\rm M}'(P)$ and integrating.

The compression modulus $K(P)$ in (16) coincides with the Murnaghan approximation $K_{\rm M}(P)$ in linear order, cf. (17). The EoS (15) is analytic at $P = 0$ and can be expanded in an ascending series,

$$\frac{\rho(P)}{\rho_0} = 1 + \frac{1}{K_0}P + \frac{1 - K_0'}{2K_0^2}P^2 + \cdots \tag{19}$$

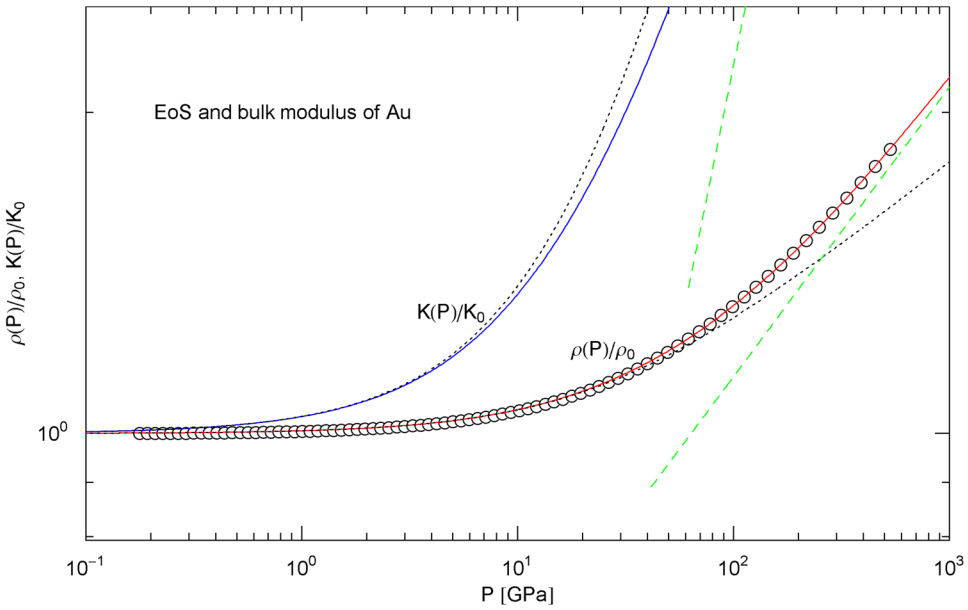

Fig. 10 Pressure isotherm at 300 K and compression modulus of gold. Data points up to 500 GPa by shock compression [27]. The χ^2 fit (solid red curve) is performed with EoS $\rho(P)$ in (15), the fitting parameters are recorded in Table 2. The solid blue curve shows the compression modulus $K(P)$, cf. (16). The dashed green lines are asymptotes and the dotted black curves depict the Murnaghan approximations

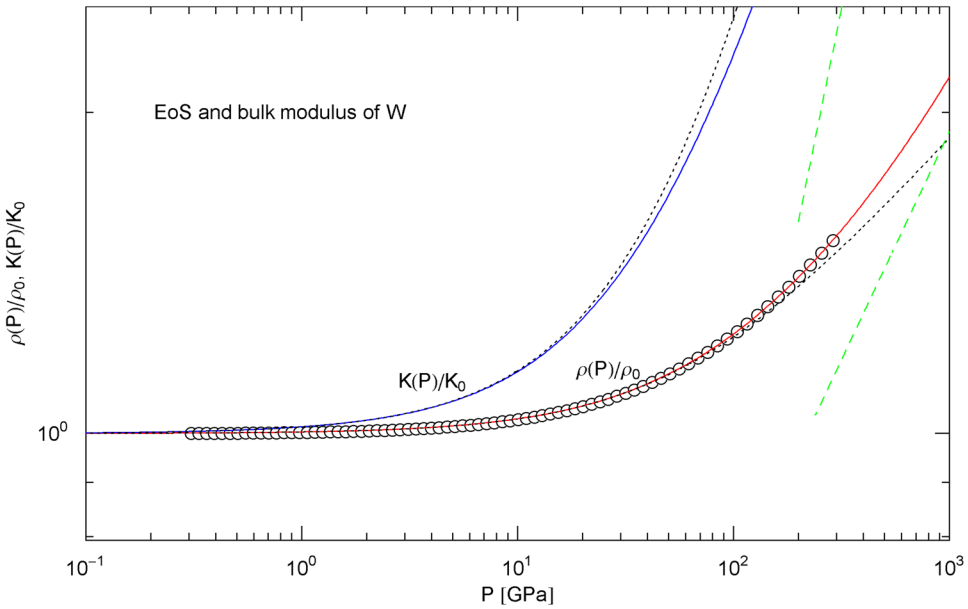

Fig. 11 Pressure isotherm at 300 K and compression modulus of tungsten. Data points up to 300 GPa by shock compression [25]. The χ^2 fit (solid red curve) is performed with EoS $\rho(P)$ in (15) and fitting parameters in Table 2. The solid blue curve is the compression modulus $K(P)$, cf. (16). The dotted black curves depict the Murnaghan EoS and the linear approximation of the compression modulus, cf. after (18). The dashed green lines are asymptotes

with K_0 and K_0' in (17), by making use of the zero pressure identities $(\rho(P)/\rho'(P))_{|P=0} = K_0$ and $(\rho(P)/\rho'(P))'_{|P=0} = K_0'$. The Murnaghan EoS admits the same second-order expansion. As is evident from Figs. 6, 7, 8, 9, 10, 11 and 12, a linear compression modulus is quite accurate up to about 5 GPa, and the Murnaghan approximation of EoS (15) remains valid up to about 50 GPa.

In the opposite high-pressure regime, the leading order of EoS (15) is a power law,

$$\rho(P) \sim a_\infty P^{\alpha_\infty}, \quad \alpha_\infty := \frac{1}{\hat{K}_0'} + \sum_{k=2}^{n} \eta_k,$$
$$a_\infty := \rho_0 \left(\frac{\hat{K}_0'}{\hat{K}_0}\right)^{1/\hat{K}_0'} \prod_{k=2}^{n} b_k^{-\eta_k}, \tag{20}$$

and it is convenient to write $\Delta(P)$ in (16) as

$$\Delta(P) = \hat{K}_0' \left(1 + \frac{\hat{K}_0}{\hat{K}_0' P}\right) \sum_{k=2}^{n} \frac{\eta_k}{1 + b_k/P}, \tag{21}$$

which converges to a constant at high pressure, $\Delta(P) = \hat{K}_0' \sum_{k=2}^{n} \eta_k + \mathrm{O}(1/P)$. The corresponding asymptotic

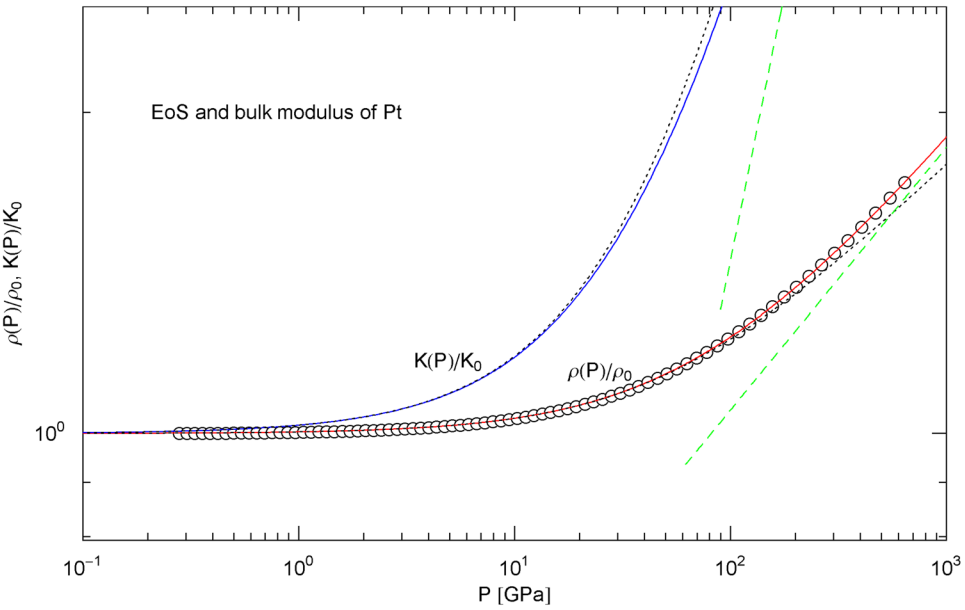

Fig. 12 Pressure isotherm and compression modulus of platinum. Data points up to 660 GPa by shock compression [27]. The χ^2 fit (solid red curve) is performed with EoS $\rho(P)$ in (15), the fitting parameters are recorded in Table 2. The solid blue curve shows the compression modulus $K(P)$, cf. (16). The dashed green lines are asymptotes and the dotted black curves depict the Murnaghan approximations, cf. after (18)

Table 2 Fitting parameters of the pressure isotherms of Al, Cu, Mo, Ta, Au, W and Pt, at ambient temperature of 300 K. The isothermal EoS used for the fits is defined in (15)

	Al	Cu	Mo	Ta	Au	W	Pt	Cu @ TPa
ρ_0[g/cm^3]	2.707	8.939	10.22	16.67	19.24	19.25	21.41	8.939
K_0[GPa]	73	133.5	264.87	194	166.7	296	280.03	133.5
K_0'	4.42	5.36	3.7499	3.83	6.23	4.3	5.0886	5.36
b_2[GPa]	78.084	120.03	612.12	90.405	114.00	531.46	169.13	113.31
η_2	0.13699	0.14094	0.14521	0.28648	0.17773	0.25268	0.10226	0.13916
b_3[GPa]	–	–	–	–	–	–	–	6507.1
η_3	–	–	–	–	–	–	–	0.15077
$\hat{K}_0$[GPa]	83.723	158.32	282.63	503.58	225.24	344.48	337.11	160.28
$\hat{K}_0'$	5.6564	7.2929	4.2386	16.918	10.680	5.7177	6.9681	7.4471
χ^2	6.06×10^{-5}	2.53×10^{-5}	1.68×10^{-5}	1.02×10^{-4}	7.75×10^{-5}	1.27×10^{-5}	5.00×10^{-7}	5.40×10^{-4}
dof	82	82	84	80	81	75	78	112
SE	1.04×10^{-3}	6.37×10^{-4}	6.88×10^{-4}	1.34×10^{-3}	1.06×10^{-3}	4.34×10^{-4}	1.12×10^{-4}	6.57×10^{-3}
$1-R^2$	2.26×10^{-5}	8.56×10^{-6}	6.23×10^{-6}	5.22×10^{-5}	2.76×10^{-5}	1.20×10^{-5}	4.21×10^{-7}	3.57×10^{-5}

The mass density ρ_0, cf. Ref. [25], and the bulk modulus K_0 at zero pressure and its pressure derivative K_0' inferred from ultrasonic measurements [54–65] are taken as input parameters. In the case of Mo and Pt, K_0' is treated as fitting parameter, for lack of acoustic measurements. Otherwise, there are only two fitting parameters in EoS (15) (with $n = 2$), the amplitude b_2 and exponent η_2 defining the second factor of the EoS. The pressure isotherms are depicted in Figs. 6, 7, 8, 9, 10, 11 and 12, covering pressures up to a few hundred GPa (subject to availability of data points). In the last column, we have indicated the parameters of the EoS of copper extended to pressures up to 60 TPa with high-pressure data points from DFT calculations [28], see Fig. 13. In this case, a third factor in EoS (15) can be specified ($n = 3$), depending on two additional fitting parameters b_3 and η_3. Also listed are the constants $\hat{K}_0$ and $\hat{K}_0'$ defining the first factor of the EoS (15), which are calculated from the input and fitting parameters according to (17) and (18). The minimum of the least-squares functional χ^2, the degrees of freedom (dof), the standard error SE and determination coefficient R^2 (see the caption to Table 1) of the least-squares fits in Figs. 6, 7, 8, 9, 10, 11, 12 and 13 are recorded as well

limits of the compression modulus (16) and its derivative are $K(P) = K_\infty' P + \mathrm{O}(1)$ and $K'(P) = K_\infty' + \mathrm{O}(1/P^2)$, where $K_\infty' = K'(P)_{|P\to\infty} = 1/\alpha_\infty$ with $\alpha_\infty(\hat{K}_0', \eta_k) = 1/\hat{K}_0' + \sum_{k=2}^{n} \eta_k$ as defined in (20).

The EoS $\rho(P) \propto P^{3/5}$ of a non-relativistic degenerate electron gas in the Thomas–Fermi free-electron approximation gives $K_\infty' = 5/3$ [51, 66], leading to the condition $\alpha_\infty(\hat{K}_0', \eta_k) = 3/5$ to be satisfied by the exponents $\hat{K}_0'$ and η_k in (15) and (20). Application of this relation to the EoS of copper depicted in Fig. 13 (which is accurate up to 60 TPa and based on EoS (15) with $n = 3$ and parameters in Table 2) suggests that an additional factor $\left(1 + P/b_4\right)^{\eta_4}$ with

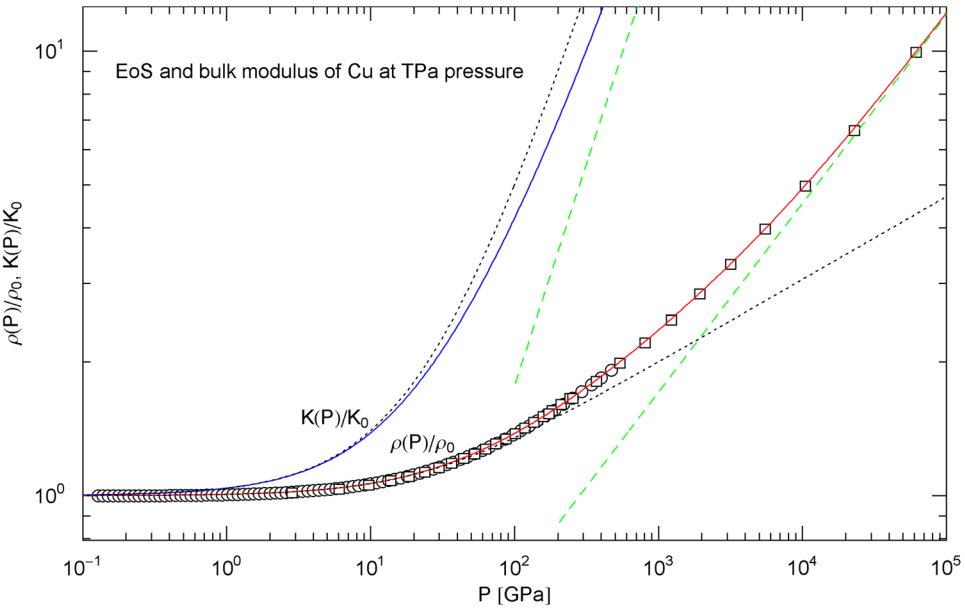

Fig. 13 Pressure isotherm at 300 K and compression modulus of copper up to 60 TPa. Data points up to 450 GPa (circles) obtained by shockless compression [26] and up to 60 TPa (squares) from DFT calculations [28]. The χ^2 fit (solid red curve) is performed with the isothermal EoS $\rho(P)$ in (15) (with $n = 3$), the fitting parameters are listed in Table 2. The solid blue curve shows the compression modulus $K(P)$, cf. (16). The dotted black curves depict the Murnaghan EoS and the linear compression modulus derived from it, cf. after (18). The dashed green straight lines indicate the asymptotes of the pressure isotherm and compression modulus

$\eta_4 \approx 0.176$ will be necessary in EoS (15) ($n = 4$) to extend the density–pressure curve beyond 60 TPa. (In the case of an ultra-relativistic degenerate electron plasma, $K'_\infty = 5/3$ is replaced by $K'_\infty = 4/3$, so that $\alpha_\infty = 3/4$.) Phenomenological thermodynamic arguments were used in Refs. [67, 68] to suggest the inequality $K'_\infty > 5/3$ instead of $K'_\infty = 5/3$. In contrast to the positivity of the heat capacities and compressibilities, this is not a necessary equilibrium condition but presumably more realistic for planetary cores than the Thomas–Fermi limit [5, 69]. The inequality $K'_\infty > 5/3$ weakens the above condition to $\alpha_\infty(\hat{K}'_0, \eta_k) < 3/5$ and gives the constraint $\eta_4 < 0.176$ on the exponent of the fourth factor in the ultra-high pressure EoS of copper applicable beyond 60 TPa.

4 Conclusion

The examples discussed in Sects. 2 and 3 demonstrate the efficiency of multiply broken power laws in modeling empirical equations of state of solids. The heat capacities $C_V(T)$ and mass densities $\rho(P)$ defined in Sect. 1 are analytic functions composed of power-law segments joint by smooth analytic transitions; they do not involve series expansions, being assembled as products of power-law factors $(1 + (x/b_k)^{\beta_k/|\eta_k|})^{\eta_k}$, $k = 1, \ldots, n$, cf. (1) and (2), where x stands for the temperature or pressure variable. Broken power laws are particularly suitable to model data sets where pressure or temperature varies over several orders of magnitude, interpolating between different asymptotic regimes. The condition $b_k << b_{k+1}$ on the amplitudes defining the power-law factors allows us to systematically assemble caloric and isothermal EoSs over an ever increasing temperature or pressure range; since $b_k << b_{k+1}$, the factor with amplitude b_{k+1} does not significantly affect the EoS in the range $x \leq b_k$.

In Sect. 2, we discussed three examples of caloric EoSs (of two carbon allotropes and vitreous SiO_2); the corresponding isochoric heat capacities exhibit very different low-temperature power-law scaling and also deviate noticeably from the Debye theory in the intermediate temperature range. The log–log plots in Figs. 1, 2 and 3 depict least-squares fits of the heat capacities [modeled as broken power laws, cf. (3), (7) and (8)] to the respective isochoric data sets of diamond, graphite and v - SiO_2. For these materials, heat capacity measurements (including the conversion from isobaric to isochoric heat capacities by way of Grüneisen parameter and thermal expansion coefficient) are available over an extended temperature range covering the low- and high-temperature regimes. As these examples demonstrate, broken power laws are sufficiently adaptable to accurately reproduce the heat capacities over the full empirical temperature range, including features such as the boson peak of the glass in Fig. 4 emerging at around 10 K or the excess heat capacity (as compared to the Debye theory) of diamond peaking at 200 K, cf. Figs. 1 and 4. The analytic heat capacities obtained from the least-squares fits can be temperature integrated to obtain the caloric EoS and entropy variable, see Fig. 5.

In Sect. 3, we discussed isothermal EoSs of specific metals, capable of reproducing high-pressure data sets. The examples studied cover a wide range of mass densities (at ambient pressure), from Al to Pt, cf. Table 2. In contrast to the multiply broken power laws modeling the heat capacities in Sect. 2, which are non-analytic at $T = 0$, we used broken power laws analytic at zero pressure, cf. (2). The EoS can

then be made to converge to the Murnaghan EoS in the low-pressure regime, where the compression modulus is known to vary linearly with pressure. The least-squares fits of the isothermal EoS (15) to high-pressure data sets of Al, Cu, Mo, Ta, Au, W and Pt are depicted in Figs. 6, 7, 8, 9, 10, 11 and 12. In all cases, the fits are uniformly accurate over the full empirical pressure range, from ambient pressure to several hundred GPa. In Fig. 13, the empirical EoS of Cu is extended into the TPa regime, using data points from DFT calculations for the least-squares regression. In Sect. 3, we also explained the implementation of the ultra-high pressure Thomas–Fermi limit into empirical isothermal EoSs defined by multiply broken power laws.

References

1. W.B. Holzapfel, High Press. Res. **16**, 81 (1998)
2. W.B. Holzapfel, Z. Kristallogr. **216**, 473 (2001)
3. J.S. Tse, W.B. Holzapfel, J. Appl. Phys. **104**, 043525 (2008)
4. J. Hama, K. Suito, J. Phys. Condens. Matter **8**, 67 (1996)
5. F.D. Stacey, Rep. Prog. Phys. **68**, 341 (2005)
6. R. Tomaschitz, Physica A (2020). https://doi.org/10.1016/j.physa.2019.123188
7. R. Tomaschitz, Physica A **483**, 438 (2017)
8. R. Tomaschitz, Fluid Phase Equilib. **496**, 80 (2019)
9. K.V. Khishchenko, J. Phys: Conf. Ser. **946**, 012082 (2018)
10. K.V. Khishchenko, J. Phys. Conf. Ser. **1147**, 012001 (2019)
11. K.V. Khishchenko, Tech. Phys. Lett. **30**, 829 (2004)
12. D.V. Minakov, P.R. Levashov, K.V. Khishchenko, AIP Conf. Proc. **1426**, 836 (2012)
13. D.V. Minakov, P.R. Levashov, K.V. Khishchenko, V.E. Fortov, J. Appl. Phys. **115**, 223512 (2014)
14. M.A. Kadatskiy, K.V. Khishchenko, J. Phys: Conf. Ser. **653**, 012079 (2015)
15. M.A. Kadatskiy, K.V. Khishchenko, J. Phys. Conf. Ser. **774**, 012005 (2016)
16. M.A. Kadatskiy, K.V. Khishchenko, Phys. Plasmas **25**, 112701 (2018)
17. K.V. Khishchenko, J. Phys. Conf. Ser. **121**, 022025 (2008)
18. K.V. Khishchenko, J. Phys. Conf. Ser. **653**, 012081 (2015)
19. J.R. Macdonald, Rev. Mod. Phys. **38**, 669 (1966)
20. B.G. Yalcin, Appl. Phys. A **122**, 456 (2016)
21. S. Khatta, S.K. Tripathi, S. Prakash, Appl. Phys. A **123**, 582 (2017)
22. M. Kaddes, K. Omri, N. Kouaydi, M. Zemzemi, Appl. Phys. A **124**, 518 (2018)
23. W. Ouerghui, M.S. Alkhalifah, Appl. Phys. A **125**, 374 (2019)
24. A. Laroussi, M. Berber, B. Doumi, A. Mokaddem, H. Abid, A. Boudali, H. Bahloul, H. Moujri, Appl. Phys. A **125**, 676 (2019)
25. A.D. Chijioke, W.J. Nellis, I.F. Silvera, J. Appl. Phys. **98**, 073526 (2005)
26. R.G. Kraus, J.-P. Davis, C.T. Seagle, D.E. Fratanduono, D.C. Swift, J.L. Brown, J.H. Eggert, Phys. Rev. B **93**, 134105 (2016)
27. Y. Wang, R. Ahuja, B. Johansson, J. Appl. Phys. **92**, 6616 (2002)
28. C.W. Greeff, J.C. Boettger, M.J. Graf, J.D. Johnson, J. Phys. Chem. Solids **67**, 2033 (2006)
29. L.E. Fried, W.M. Howard, Phys. Rev. B **61**, 8734 (2000)
30. K.V. Khishchenko, V.E. Fortov, I.V. Lomonosov, M.N. Pavlovskii, G.V. Simakov, M.V. Zhernokletov, AIP Conf. Proc. **620**, 759 (2002)
31. K.V. Khishchenko, V.E. Fortov, I.V. Lomonosov, Int. J. Thermophys. **26**, 479 (2005)
32. S.Sh. Rekhviashvili, Kh.L. Kunizhev, High Temp. **55**, 312 (2017)
33. J.E. Desnoyers, J.A. Morrison, Philos. Mag. **3**, 42 (1958)
34. W. DeSorbo, J. Chem. Phys. **21**, 876 (1953)
35. A.C. Victor, J. Chem. Phys. **36**, 1903 (1962)
36. B.J.C. van der Hoeven, P.H. Keesom, Phys. Rev. **130**, 1318 (1963)
37. W. DeSorbo, G.E. Nichols, J. Phys. Chem. Solids **6**, 352 (1958)
38. W. DeSorbo, W.W. Tyler, J. Chem. Phys. **21**, 1660 (1953)
39. M.W. Chase, NIST-JANAF *Thermochemical Tables*, 4th ed. (AIP, Woodbury, 1998), https://janaf.nist.gov
40. A.T.D. Butland, R.J. Maddison, J. Nucl. Mater. **49**, 45 (1973)
41. T. Nihira, T. Iwata, Phys. Rev. B **68**, 134305 (2003)
42. V.N. Senchenko, R.S. Belikov, J. Phys: Conf. Ser. **891**, 012338 (2017)
43. J.C. Lasjaunias, A. Ravex, M. Vandorpe, S. Hunklinger, Solid State Commun. **17**, 1045 (1975)
44. R.O. Pohl, in: *Amorphous Solids*, W.A. Phillips, ed. (Springer, Berlin, 1981)
45. R.B. Stephens, Phys. Rev. B **8**, 2896 (1973)
46. P. Flubacher, A.J. Leadbetter, J.A. Morrison, B.P. Stoicheff, J. Phys. Chem. Solids **12**, 53 (1959)
47. R.C. Lord, J.C. Morrow, J. Chem. Phys. **26**, 230 (1957)
48. P.W. Anderson, B.I. Halperin, C.M. Varma, Philos. Mag. **25**, 1 (1972)
49. W.A. Phillips, Rep. Prog. Phys. **50**, 1657 (1987)
50. I.S. Gradshteyn, I.M. Ryzhik, *Table of Integrals, Series, and Products*, 8th edn. (Academic Press, Waltham, 2015)
51. W.B. Holzapfel, Rep. Prog. Phys. **59**, 29 (1996)
52. W.B. Holzapfel, High Press. Res. **22**, 209 (2002)
53. G.M. Amulele, M.H. Manghnani, S. Marriappan, X. Hong, F. Li, X. Qin, H.P. Liermann, J. Appl. Phys. **103**, 113522 (2008)
54. A. Dewaele, P. Loubeyre, M. Mezouar, Phys. Rev. B **70**, 094112 (2004)
55. W.B. Holzapfel, High Press. Res. **30**, 372 (2010)
56. K. Katahara, M. Manghnani, E. Fisher, J. Appl. Phys. **47**, 434 (1976)
57. K.W. Katahara, M.H. Manghnani, E.S. Fisher, J. Phys. F: Met. Phys. **9**, 773 (1979)
58. P. van't-Klooster, N.J. Trappeniers, S.N. Biswas, Physica B + C **97**, 65 (1979)
59. S.N. Biswas, P. van't-Klooster, N.J. Trappeniers, Physica B + C **103**, 235 (1981)
60. J.L. Tallon, A. Wolfenden, J. Phys. Chem. Solids **40**, 831 (1979)
61. D. Steinberg, J. Phys. Chem. Solids **43**, 1173 (1982)
62. W. Holzapfel, M. Hartwig, W. Sievers, J. Phys. Chem. Ref. Data **30**, 515 (2001)
63. K. Syassen, W.B. Holzapfel, J. Appl. Phys. **49**, 4427 (1978)
64. K. Takemura, A. Dewaele, Phys. Rev. B **78**, 104119 (2008)
65. W.B. Holzapfel, M.F. Nicol, High Press. Res. **27**, 377 (2007)
66. E.E. Salpeter, Astrophys. J. **134**, 669 (1961)
67. F.D. Stacey, Geophys. J. Int. **143**, 621 (2000)
68. F.D. Stacey, P.M. Davis, Phys. Earth Planet. Inter. **142**, 137 (2004)
69. F.D. Stacey, J.H. Hodgkinson, Phys. Earth Planet. Inter. **286**, 42 (2019)